PHYSICAL REVIEW B **105**, 245107 (2022)

Role of spin-orbit coupling in canted ferromagnetism and spin-wave dynamics of $SrRuO_3$

Kyo-Hoon Ahn,[1,2] Alberto Marmodoro,[1] Jiří Hejtmánek,[1] Zdeněk Jirák,[1] and Karel Knížek[1]
[1]*Institute of Physics of the CAS, Cukrovarnická 10, 162 00 Praha 6, Czech Republic*
[2]*Division of Display and Semiconductor Physics, Korea University, Sejong 30019, Korea*

(Received 22 December 2021; revised 19 May 2022; accepted 20 May 2022; published 8 June 2022)

A canted ferromagnetic arrangement with a long-range-ordered antiferromagnetic component is predicted for the metallic $SrRuO_3$ orthoperovskite based on local-density-approximation-type electronic-structure calculation including on-site Coulomb repulsion U and spin-orbit coupling. The electronic state of Ru^{4+} ions and the nature of nonzero orbital momentum are analyzed in detail. With regard to the density of states at the Fermi level, the value of the magnetic moment, and the easy axis along the a-axis in a *Pbnm* setting, a good agreement with the experimental data is achieved for $U = 1$ eV. The calculated parameters of magnetic exchange, including the anisotropic and antisymmetric terms, are used to determine the magnon spectra. It is shown that notable anisotropic exchange in $SrRuO_3$ is responsible for a gap of 1.7 meV at the Γ point of the magnon spectra, found previously by inelastic neutron diffraction. The origin of the spin canting that is confined within the ab-plane follows from the presence of the Dzyaloshinskii-Moriya interaction associated with the antisymmetric exchange.

DOI: 10.1103/PhysRevB.105.245107

I. INTRODUCTION

Spin-orbit coupling (SOC) is at the root of distinct physical phenomena such as anisotropic or antisymmetric exchange interactions, magnetoelectric and spin Hall effects, Fermi-surface topology, etc. It has been adopted to explain the electrical and magnetic properties of various materials in the past several decades. Concurrently, there has been a revival of interest in the canting of spin magnetic moments in oxides with late transition metal (TM) ions, since the SOC plays an important role in such systems: it couples not only the spin and the orbital momentum of the $5d$ electrons, but also the spin and the lattice degree of freedoms. One of the most famous examples is the weak ferromagnetism in the antiferromagnetic insulator Sr_2IrO_4 [1]. This magnetic feature has been explained by the lattice distortion, showing that the canting angle is nearly identical to the tilting angle of the IrO_6 octahedra [2].

In the current study, we identify $SrRuO_3$ as an opposite counterpart, representing weak antiferromagnetism in ferromagnetic metal. Although the effects of SOC are weaker in the case of Ru $4d$ compared to Ir $5d$, the presence of a spin-canted phase in $SrRuO_3$ has already been speculated on based on the Dzyaloshinskii-Moriya interaction (DMI) [3]. More direct support comes from calculations evidencing a deviation of the orbital moment from the ferromagnetic axis while keeping the parallel alignment of the spin moments [4]. This approach showed, however, only a tiny canting angle of total moments 1.3°–1.7°. As an important advancement, the present results are based on the noncollinear density-functional theory plus on-site Coulomb repulsion U. They also take into account an additional contribution to spin canting due to the orthorhombic distortion [2], and they clearly demonstrate that magnetic moment canting is favored over the collinear arrangement. The spin-canted ferromagnet $SrRuO_3$ of metallic conduction can thus be considered as a candidate for possible realization of the chiral Hall effect [5,6].

$SrRuO_3$ is a ferromagnetic metal with Curie temperature $T_c = 165$ K and magnetic moment $1.69\mu_B$ with the easy-axis in the a-direction [7,8]. Its perovskite structure displays orthorhombic *Pbnm* symmetry with four formula units $SrRuO_3$ in the unit cell. The distortion from the ideal cubic perovskite structure occurs due to double tilt (so-called buckling) of RuO_6 octahedra, in which each octahedron is rotated by 6° along the cubic [001] axis and inclined to 8°–9° by rotation along the [110] axis [9–14]. The octahedra themselves remain practically regular, with Ru-O bond lengths within 1.98–1.99 Å, nevertheless a small deviation 1° of the O-Ru-O angle from the ideal 90° is present in the ab-plane. This results in an anomalous ratio of the lattice parameters $a > b$, which is opposite to the predictions of the Glazer structural description for *Pbnm* supposing regular octahedra [15]. As the origin of this distortion, a weak Jahn-Teller effect of t_{2g} orbitals was tentatively proposed [14].

With regard to the temperature evolution of $SrRuO_3$ structure, the most important structural data obtained by high-resolution neutron diffraction [13,14] indicate that, upon further cooling below T_c, the Ru-O distances do not show any common shortening, rather they seem to increase slightly. In lattice parameters, an abrupt change of thermal expansion coefficients is observed, and so the sample volume remains practically constant below $T_c = 165$ K, thus recalling the Invar effect in Fe-Ni alloys [14,16,17]. Since tilting angles do not show any anomaly at T_c, and the distorted O-Ru-O angle in the ab-plane is not changed at all, the origin of the Invar behavior of $SrRuO_3$ remains unclear.

Inelastic neutron scattering (INS) and neutron Brillouin scattering (NBS) have been applied to investigate the spin-wave dynamics. The NBS experiment performed on a powder sample of $\mathrm{SrRuO_3}$ has shown a dispersion of standard quadratic form starting at the Γ point with an energy gap $\Delta \sim 2$ meV. The stiffness constant D_{stiff} amounts to 62 meVÅ^2 at low temperature and decreases with increasing temperature down to zero at T_{c} [18,19]. The magnon gap exhibits only a weak and nonmonotonous temperature dependence. It is proposed that such a property comes from a small contribution of Weyl fermions to the spin anisotropy energy, and that this contribution is proportional to the anomalous Hall effect; see also [20].

The temperature dependence of magnon dispersion of $\mathrm{SrRuO_3}$ single crystal has been studied by INS in [8]. It is observed that the magnon modes display substantial broadening, indicating a strong interaction with charge carriers. The nonmonotonous temperature dependence of both the magnon gap and the stiffness constant, which follows that of the anomalous Hall effect, has also been observed. The low-temperature stiffness constant $D_{\mathrm{stiff}} = 87(2)$ meVÅ^2 and the energy gap $\Delta = 0.94(3)$ meV are determined. Another study of the $\mathrm{SrRuO_3}$ magnon spectra has been performed on epitaxial films [21]. A substantially smaller magnon gap of $\Delta = 0.32$ meV is reported. Several possible sources of this smaller gap, such as the higher-symmetry tetragonal structure imposed by the interfacial strain and the impurity levels due to Ru and O vacancies, have been discussed.

In what follows, we focus on the determination of the canted FM state of $\mathrm{SrRuO_3}$ using the LDA+U+SOC method, a detailed characterization of $4d$ electronic states at $\mathrm{Ru^{4+}}$ sites with eigenvectors and occupation numbers specified, and the calculation of tensors describing the anisotropic and antisymmetric exchange interactions and subsequent derivation of magnon spectra in $\mathrm{SrRuO_3}$.

Orbital effects of t_{2g} electrons

In the present case of the metallic ferromagnet $\mathrm{SrRuO_3}$, the electric conduction is dominated by electrons in the partially occupied spin-down band of $\mathrm{Ru}(t_{2g}) - \mathrm{O}(\pi)$ origin, while the spin-up band is practically full. The electronic state in the atomic sphere of $\mathrm{Ru^{4+}}$ can be viewed, by applying the model of a strong crystal field, as one $t_{2g}(\downarrow)$ electron outside the fully occupied $t_{2g}^3(\uparrow)$ shell. In a regular $\mathrm{RuO_6}$ octahedron, the single t_{2g} electron thus appears in triple orbital degeneracy, and it is described by a mixed quantum state with equal populations of three orthonormal wave functions making the basis of the t_{2g} space—the d_{xy}, d_{yz}, and d_{xz} triplet being one possible choice. Such a mixed quantum state is characterized by a cubic distribution of electron density as illustrated later in Fig. 5.

Ionic triplets may be conveniently described as states with fictitious angular momentum quantum number $\tilde{L} = 1$ [22]. Considering then the free-ion origin of t_{2g} states, the most obvious (commonly known) eigenstates are $\psi_1 = 1/\sqrt{2}(d_{yz} + i.d_{xz})$, $\psi_0 = d_{xy}$, and $\psi_{-1} = 1/\sqrt{2}(d_{yz} - i.d_{xz})$ characterized by $\tilde{L}_z = 1$, 0, and -1, respectively. The triplet orbital degeneracy can be lifted by Jahn-Teller or spin-orbit coupling effects. In the former case, a singlet orbital state of anisotropic electron density is stabilized by a spontaneous distortion of the octahedron that can be of e_g and t_{2g} character. Some examples of the Jahn-Teller effect, represented by real-valued wave functions, are given in the upper row of Fig. 1. They are coupled with distortions of three types: (a) tetragonal stretching, (b) trigonal shear, and (c) orthorhombic shear. Note that only the variants (a) and (b) and their symmetrical equivalents can become ground states of the Jahn-Teller effect in systems with T_{2g} or T_{1g} ions in strictly regular octahedra (see, e.g., [23]).

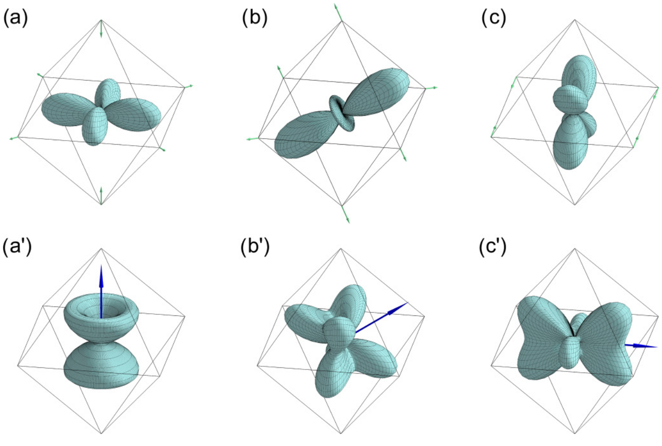

FIG. 1. Upper row: Examples of the Jahn-Teller stabilized eigenstates and their associated octahedral distortion (red arrows). (a) $\psi_0 = d_{xy}$ in the $t_{2g} \otimes e_g$ effect, and (b) $\psi_0 = 1/\sqrt{3}(d_{xy} + d_{yz} + d_{xz})$, (c) $\psi_0 = 1/\sqrt{2}(d_{yz} - d_{xz})$ in two kinds of the $t_{2g} \otimes t_{2g}$ effect. Lower row: Complementary states making a doublet of unquenched orbital momenta (blue arrows). (a′) $\psi_1 = \psi_{-1}^* = 1/\sqrt{2}(d_{yz} + i.d_{xz})$ with $\tilde{L}_z$ along [001], (b′) $\psi_1 = \psi_{-1}^* = 1/\sqrt{3}(d_{xy} + e^{i2\pi/3} d_{yz} + e^{-i2\pi/3} d_{xz})$ with $\tilde{L}_z$ along [111], and (c′) $\psi_1 = \psi_{-1}^* = 1/\sqrt{3}[d_{xy} + i.(d_{yz} + d_{xz})]$ with $\tilde{L}_z$ along [110].

Lifting of triple degeneracy by SOC is a more complex phenomenon. Instead of the stabilization of the singlet state, a complementary doublet state is stabilized by octahedron distortion of opposite sign, with an energy gain of half of that for the Jahn-Teller effect. Nonetheless, the orbital momentum of doublets is not quenched, and additional energy is gained by SOC, leading to a preference over the purely electrostatic Jahn-Teller effect [24,25]. Illustrative examples of such doubly degenerate states, represented by a pair of complex-conjugated wave functions with the same electron density distribution but opposite orbital momenta, are given in the lower row of Fig. 1. Each of the doublets in (a′), (b′), or (c′), with the corresponding singlet (a), (b), or (c) added, can be considered as a distinct realization of the t_{2g} triplet with fictitious $\tilde{L}_z = \pm 1$, 0.

All of the above-mentioned description and dominance of the SOC effect applies primarily to localized electrons in systems with T_{2g} or T_{1g} ions. We will show later that also in the present case of metallic $\mathrm{SrRuO_3}$, the $4d$ electronic states within the $\mathrm{Ru^{4+}}$ centered Wannier function exhibit a similar effect, where energy gain is achieved mainly by eigenvectors with unlike occupation of $\tilde{L}_z = 1$ and -1 and therefore some nonzero momentum, while total electron density remains very close to the ideal cubic distribution.

II. COMPUTATIONAL METHOD

Density-functional theory (DFT) calculations using the Vienna *ab-initio* simulation (VASP) package [26,27] were carried out with a k-mesh of $12\times12\times8$ points and a plane-wave cutoff of 600 eV. The projector-augmented wave (PAW) [28] potentials with the local density approximation (LDA) [29] were used. The DFT+U approach was applied to the d-shells of the Ru sites with $U = 1$ eV and $J_H = 0.6$ eV, with the around mean-field (AMF) scheme [30] for computing double-counting correction.

The fully unconstrained noncollinear calculations [31] are performed to examine the canting of the local spin directions due to the spin-orbit-coupling (SOC) effects. The orthorhombic cell is described according to the neutron diffraction experiments at 1.5 K [13].

To explore the detailed spin dynamics, a tight-binding model is constructed from the DFT bands using the WANNIER90 [32] package, including the Ru-d, O-p, and Sr-d characters as a basis set. The magnetic exchange parameters include the isotropic exchange J^{iso}, the anisotropic exchange $\mathbf{J}^{\text{ani}}$, and the Dzyaloshinskii-Moriya interaction computed by TB2J code [33] with a dense k-mesh of $24\times24\times16$ points. The maximum distance for calculating the exchange parameters is set to 10 Å. The magnetization curves are calculated using the Depondt-Mertens method [34] implemented in MULTIBINIT code [35,36], with a sufficiently large supercell of $20\times20\times20$ unit cells. The adiabatic magnon spectra are obtained by SPINW code [37] through the linear spin-wave theory [38].

The main results of the calculations are presented in Secs. III A and III B, and other important data concerning the spin-up and spin-down density of states (see also the similar result of Fang *et al.* [20]), details of the Ru^{4+} centered Wannier function, the density, and parameters influencing the magnon dispersion are available in the supplemental material [39].

III. RESULTS AND DISCUSSION

A. Magnetic ground state of SrRuO$_3$

In the first step, we examined the possible canting of the ferromagnetic spin moments by the LDA+U+SOC calculations. The initial direction of the spins was subsequently aligned with the a, b, and c axes of *Pbnm*, and the noncollinear spin configuration was refined for the values of $U = 0.6$–3 eV. At the end of the refinement, each of the local spins was slightly inclined by 2°–5° from the initial direction depending on the value of U, whereas the net moment remained along the initial axis.

The resulting energy differences of the canted configurations are compared in Fig. 2, where the noncollinear configurations are labeled NCLa, NCLb, and NCLc for the net moment along the a, b, and c axis, respectively. The energy of the collinear configuration along the experimentally determined easy-axis a (CLa) is set to zero. The NCLa phase has about 0.6 meV/f.u. lower energy than the CLa one for the whole range of U. The energies of the NCL configurations along b and c are also always lower than that of the CL configuration. The configuration with the lowest energy is NCLa for smaller values of $U \leqslant 1.1$ eV, i.e., the theoretical easy-axis is along the a-direction, whereas for larger $U > 1.1$ eV the NCLb configuration has the lowest energy and the theoretical easy-axis would be along the b-direction.

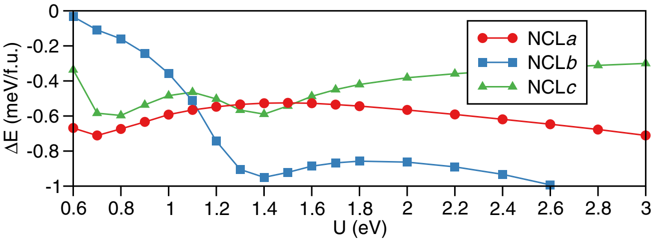

FIG. 2. Energy difference plots with various values of U, including SOC, of the NCLa (red circles), NCLb (blue squares), and NCLc (green triangles) phases. Here, the energy of the CLa phase is set to zero.

To find the value of U that best matches the experimental properties, we have calculated the dependence of the spin moments on U. The dependence for the NCLa configuration is displayed in Fig. 3. The spin moments of NCLb and NCLc configurations display the same dependence. The experimental value of $1.69\mu_B$ [8] is reproduced for the value of $U \approx 1$ eV, for which also the configuration NCLa is the magnetic ground state, in agreement with the experimental easy-axis a. The corresponding spin arrangement is illustrated in Fig. 4—it can be described as a combination of FM order along a, C-type AFM order along b, and G-type AFM order along c [40], i.e., the $F_xC_yG_z$ configuration allowed by *Pbnm* symmetry. The figure shows also canting angles calculated for various values of U. It is seen that local spin moments are slightly tilted (∼3° for $U = 1$ eV) in both the y and z directions.

The formation of canted spin structure is primarily due to the presence of significant SOC, thus the strong role of DMI in SrRuO$_3$, which is analogous to Sr$_2$IrO$_4$ [2]. Let us note that there is also a direct relation to the octahedral tilt. To prove this, we have performed the test calculation using the cubic perovskite structure with no octahedra rotation (Ru-O-Ru angles equal to 180°) and no octahedra deformation (O-Ru-O angles equal to 90°). In this case, the collinear ferromagnetic configuration was refined as the ground state, and all elements of the DMI tensor were found to be zero. This confirms that spin canting in metallic SrRuO$_3$ is conditioned by the octahedra rotation.

We conclude that our calculations obtained with $U = 1$ eV reproduce correctly the magnetic easy-axis and magnetic

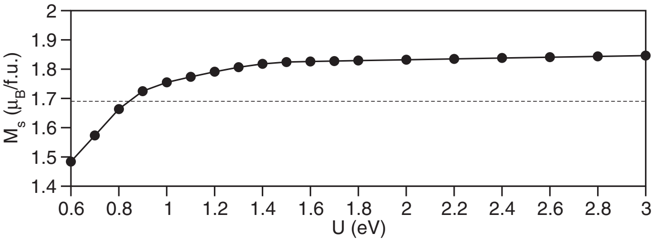

FIG. 3. Calculated spin moments of the NCLa phase, with various values of U including SOC. The experimental value is $1.69\mu_B$ [8]. The gap in the spin-up channel is opened at $U = 1.6$ eV.

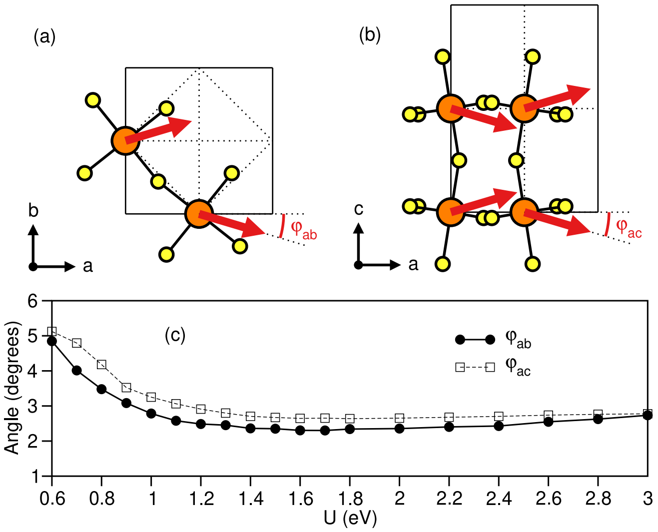

FIG. 4. Schematic view of the canted spin arrangement in the NCL*a* phase (a) on the *ab*-plane at $z = 0$ and 0.5, and (b) on the *ac*-plane. The orange (yellow) circles and the red arrows indicate the Ru (O) sites and the direction of the spin moment, respectively. The corresponding angles with various values of U are presented in (c). The orientation of spins corresponds to magnetic group symmetry $Pbm'n'$ (the dash denotes the combination of a crystallographic symmetry element with time inversion).

moment of SrRuO$_3$. By applying this value, the SrRuO$_3$ phase is characterized as a canted ferromagnet of metallic conductivity with carriers of both spins, whereas opening a gap at the Fermi level in a spin-up band can be expected only for $U \geqslant 1.6$ eV (see the supplemental material [39] for more details). In addition, the calculated density matrix for the 4d-based Wannier function allows us to determine the eigenvectors in the full Ru-4d basis (See Table S.3 in the supplemental material [39]), leading to the occupation of (0.979, 0.977, 0.975) and (0.605, 0.604, 0.600) for spin-up triplet and spin-down triplet, respectively. It appears that the t_{2g} spin-down electron in the Ru atomic sphere is in a mixed quantum state that is characterized by a cubic symmetrical distribution of electron density as seen in Fig. 5, and this property is in agreement with the magnetic density distribution of SrRuO$_3$ determined recently using polarized neutron diffraction [41].

The presently calculated state is further characterized by the nonvanishing orbital moment $g_L\tilde{\mathbf{L}} = [0.023, 0.001, 0.008]\mu_{\text{B}}$, significantly inclined with respect to the ferromagnetic easy-axis a [to 4.3°; see also Fig. 4(c)]. With regard to the much larger spin moment $g_S\mathbf{S} = [1.285, -0.063, -0.073]\mu_{\text{B}}$, it is slightly inclined from the a-axis with respect to *Pbnm* coordinates. The angle between local spin and orbital moments is 23°.

The eigenstates themselves are presented in the upper row of Fig. 5. They show some similarity with one of the previously discussed model triplets in Fig. 1, namely the variant (b, b'), and this is supported also by the fact that the orbital moment $g_L\tilde{\mathbf{L}}$ is inclined only 10° from the body diagonal of the RuO$_6$ octahedron. As a better approximation, we have constructed wave functions as complex combinations within the ideal basis d_{xy}, d_{yz}, and d_{xz}. They are added to Fig. 5 for comparison. The obvious resemblance of both the density-matrix derived and modeled triplets suggests that orbital momentum observed in SrRuO$_3$ is formed by the larger occupation of ψ_1 than ψ_{-1}, actually 0.634:0.581 (see the supplemental material [39]). The occupation ψ_0 of 0.602 is slightly less than the average of the previous ones, which can be attributed to the octahedron distortion with the rather anomalous O-Ru-O angle in the *ab* plane, decreased to ∼89°. This may mean that there is perhaps some role of the Jahn-Teller effect, but it cannot be the reason for the Invar behavior of SrRuO$_3$, since it appears below T_c without any noticeable change of the O-Ru-O angle.

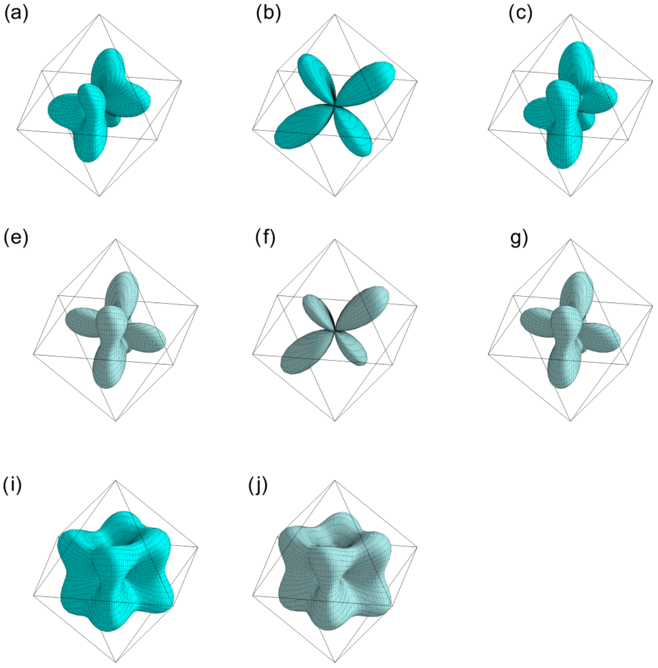

FIG. 5. Density distribution of a t_{2g} spin-down electron of Ru^{4+} in SrRuO$_3$, obtained from the 4d-based Wannier functions. Upper row: The three eigenstates derived from the calculated density matrix and its diagonalization (see the supplemental material [39]). Lower row: Rough fit (modeling) of the triplet by wave functions $\psi_1 = 2d_{xy} - (0.7 + i)d_{yz} - (0.7 - i)d_{xz}$, $\psi_0 = -0.3d_{xy} + d_{yz} + d_{xz}$, $\psi_{-1} = \psi_1^*$. Two pictures below compare the total t_{2g} spin-down density calculated for SrRuO$_3$ (left) with ideal cubic density at equal occupations of the eigenstates (right).

B. Spin dynamics

In the next step, we use the calculated exchange parameters of the effective spin Hamiltonian to explore the temperature-dependent magnetic properties of SrRuO$_3$. The general expression for total energy was used:

$$E = -\frac{1}{2}\sum_{i,j\neq i}\left[J_{ij}^{\text{iso}}\vec{S}_i\cdot\vec{S}_j + \vec{S}_i\mathbf{J}_{ij}^{\text{ani}}\vec{S}_j + \vec{D}_{ij}\cdot(\vec{S}_i\times\vec{S}_j)\right], \quad (1)$$

where J^{iso} refers to the isotropic Heisenberg exchange, the tensor $\mathbf{J}^{\text{ani}}$ refers to the anisotropic exchange, and $\vec{D}_{ij}$ is the Dzyaloshinskii-Moria interaction; see Part C of the supplemental material [39] for more details. The selected parameters calculated for nearest neighbors by LDA+U+SOC using

TABLE I. Calculated magnetic exchange parameters (in meV) for the nearest neighbors. The subscripts *ab* and *c* indicate the direction of the interactions: the former is between Ru1 at (1/2, 0, 0) and Ru2 at (0, 1/2, 0) on the *ab*-plane, while the latter is between Ru1 and Ru3 at (1/2, 0, 1/2) along the *c*-direction. J' is for the next nearest neighbors between Ru1 and Ru4 at (0, 1/2, 1/2). Here, only the diagonal elements of the anisotropic terms (J^{ani}_{xx}, J^{ani}_{yy}, J^{ani}_{zz}) are exhibited.

	J^{iso}_{ab}	J^{iso}_{c}	J'	$\mathbf{J}^{\mathrm{ani}}_{ab}$	$\mathbf{J}^{\mathrm{ani}}_{c}$	$\vec{D}_{ab}$	$\vec{D}_{c}$
CL*a*	5.319	4.201	0.134	(−0.383, −0.362, 0.063)	(0.016, −0.002, −0.932)	(−1.228, 0.166, 0.405)	(0.200, −0.803, 0.000)
NCL*a*	5.293	4.207	0.189	(−0.351, −0.514, 0.004)	(−0.204, −0.021, −0.895)	(−1.198, 0.818, 0.094)	(0.125, −0.051, 0.001)

$U = 1$ eV for CL*a* and NCL*a* configurations are displayed in Table I.

Since $\mathrm{SrRuO_3}$ displays metallic-type conductivity, the applicability of a localized spin model has to be verified. The itinerant or localized character of the magnetism can be distinguished based on the established Rhodes-Wohlfarth ratio $p_{\mathrm{eff}}/p_{\mathrm{sat}}$, where $p_{\mathrm{eff}} = gS_{\mathrm{eff}}$ corresponds to the effective Curie-Weiss moment $\mu_{\mathrm{eff}} = g\sqrt{S(S+1)}$, and $p_{\mathrm{sat}} = gS_{\mathrm{sat}}$ corresponds to the saturated magnetic moment. In the case of localized moments, the ratio $p_{\mathrm{eff}}/p_{\mathrm{sat}} = 1$ is predicted, whereas in the case of itinerant magnetism, the ratio $p_{\mathrm{eff}}/p_{\mathrm{sat}} > 1$ is predicted, increasing with decreasing ferromagnetic critical temperature T_C. For $\mathrm{SrRuO_3}$ with $T_C =$ 165 K, the ratio $p_{\mathrm{eff}}/p_{\mathrm{sat}} \sim 3$ would be expected for itinerant magnetism based on the Rhodes-Wohlfarth plot; see, e.g., Fig. 7.2. in [42]. However, according to the experimentally determined effective and saturated moments, the observed ratio $p_{\mathrm{eff}}/p_{\mathrm{sat}}$ is between 1.2 and 1.3 [43,44]. Hence, $\mathrm{SrRuO_3}$ is closer to the local magnetic moment behavior than to the itinerant, and the localized spin model is applicable. For more details regarding the quality of the Wannierization, see the supplemental material [39] and Refs. [33,45] therein.

Figure 6 shows the magnon dispersion of the NCL*a* phase calculated using the anisotropic exchange and DMI tensors (see Table I). The manifestation of the individual exchange parameters in the magnon spectra is the following. The anisotropic exchange $\mathbf{J}^{\mathrm{ani}}$ makes a small magnon gap of ∼1.7 meV at the Γ point. The isotropic exchange J^{iso} determines the stiffness constant D_{stiff} and therefore it is related to the slope of the momentum dependence of the magnon energy near the Γ point. The DMI terms make a splitting of ∼5 meV mainly at the *R* point.

Compared with the experimental results, the calculated magnon gap 1.7 meV is between the gap determined for powder sample 2 meV in [19] and the gap determined for single crystal 0.94 meV in [8]. On the other hand, the calculated stiffness constant 32.47 meVÅ^2, and thus the slope of the energy dependence, is significantly smaller than the experimental data 62 meVÅ^2 reported in [19] and 87 meVÅ^2 reported in [8].

Figure 7 shows the theoretical results of the magnetization of the NCL*a* phase. The calculated critical temperature 80 K for $U = 1$ eV is also significantly smaller than the experimental $T_{\mathrm{c}} = 165$ K. Better agreement with experimental T_{c} is achieved using $U = 2.2$ eV, however the $\mathbf{J}^{\mathrm{ani}}$ will be inappropriate due to the wrong easy-axis (Fig. 2) and also the magnetic moment would be much higher than experimentally observed (Fig. 3).

Both the critical temperature and the slope of the energy dependence are basically controlled by the stiffness constant D_{stiff}, which is related to the isotropic exchange parameter J^{iso}. One can control D_{stiff} by applying a renormalization factor η into the isotropic terms only, such as ηJ^{iso}; for more details, see the supplemental material [39].

The magnetization calculated using $\eta = 2.3$ is well fitted to $m(T) = m_0(1 - T/T_{\mathrm{c}})^{\beta}$ to reproduce the reported value of $T_{\mathrm{c}} = 165$ K, and also the renormalized stiffness constant D_{stiff}= 64.34 meVÅ^2 is in good agreement with the experimental value of 62 meVÅ^2 for the powder sample [18,19]. It is important that a single renormalization factor is sufficient to reproduce both experimental data. On the other hand, the agreement with the stiffness constant D_{stiff}= 87 meVÅ^2 determined for a single crystal in [8] would be obtained with higher η, but this will also result in too high T_{c}.

The isotropic terms J^{iso} are affected by the localization of the electron densities, hence by the strength of the on-site Coulomb parameter U. On the other hand, the anisotropic and the DMI terms are governed by the SOC effects. Table I shows the calculated magnetic exchange parameters of the CL*a* and NCL*a* phases with $U = 1$ eV. Both $\mathbf{J}^{\mathrm{ani}}_{ab}$ and $\mathbf{J}^{\mathrm{ani}}_{c}$ show a clear

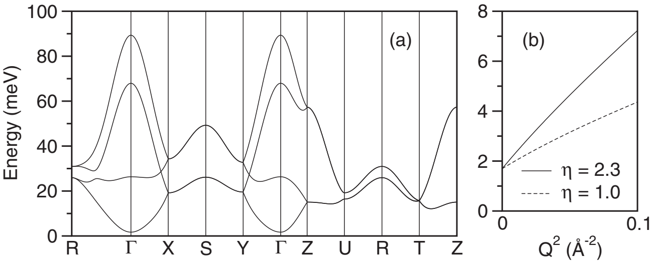

FIG. 6. Magnon dispersion of the NCL*a* phase with $U = 1$ eV (a) along the high-symmetry points in the BZ, and (b) along the Γ to *X* direction with Q^2. Here, a renormalization factor η is applied to J^{iso}.

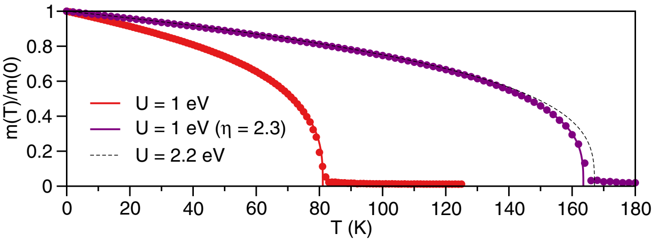

FIG. 7. Magnetization vs temperature curves of the NCL*a* phase with $U = 1$ eV (red), $U = 1$ eV and $\eta = 2.3$ (purple), and $U =$ 2.2 eV (black dashed). The corresponding parameters (T_{c}, β) are (81.1 K, 0.326), (163.6 K, 0.315), and (167.1 K, 0.314), respectively.

anisotropy between the *xx* (*yy*) and the *zz* components, which results in the magnon gap in SrRuO$_3$. The main difference between the two cases is the distribution of the DMI terms. The DMI is confined on the *ab*-plane in the NCL*a* phase, while it remains strong along the *c*-axis in the CL*a* results. Note that the isotropic interaction favors the angle between two spins as 0° or 180°, while DMI favors 90°.

The staggered rotation of $\vec{S}$ around the *a*-axis by an angle $\phi \sim \frac{1}{2}\tan^{-1}(D/\eta J^{\rm iso}) = 3.0^\circ$ [2], as a rough estimate with $|D| = 1.2$ meV, $J^{\rm iso} = (4J^{\rm iso}_{ab} + 2J^{\rm iso}_{c})/6 = 4.94$, and $\eta = 2.3$, coincides with the noncollinear result of Fig. 4.

The large-scale factor of $\eta = 2.3$, applied to the metallic ferromagnet SrRuO$_3$, can be understood as a consequence of electron correlations that generally are not reflected properly in the DFT method. Namely, the dynamical mean-field theory (DMFT) methods [46–48] indicate that the bandwidth from the DFT is about two times larger than the realistic one. In other words, the ω dependence on the self-energy $\Sigma(\omega)$, which will induce a bandwidth renormalization, is absent in the static mean-field theory such as DFT+U. Since the ratio of the bandwidth W and the strength of U are important, it is the origin of the underestimation of $J^{\rm iso}$ in our results with $U = 1$ eV. Let us note that in insulating antiferromagnet SrMnO$_3$ [49], which possesses a similar *Pbnm* perovskite structure, the analogous calculations have shown about three times larger magnitudes of exchange integrals, and the experimental $T_N = 250$ K has been reproduced without any need for renormalization [33].

C. Magnon heat capacity

In this section, we discuss the effects of the magnon gap on the specific heat. First, let us consider an ideal ferromagnet at low temperature at zero external magnetic field. When dealing with spin wave excitations of small momenta only (long wavelengths), the dispersion relation can be simplified as

$$E(Q) = \Delta + D_{\rm stiff}Q^2, \tag{2}$$

where Δ is the anisotropy gap, $D_{\rm stiff}$ is the spin-stiffness constant, and Q is the wave vector. The internal energy of a magnon in thermal equilibrium at temperature T is given by [50]

$$U_{\rm mag} = \frac{k_{\rm B}T}{4\pi^2}\left(\frac{k_{\rm B}T}{D_{\rm stiff}}\right)^{3/2}\int\frac{x^{3/2}}{e^x - 1}dx, \tag{3}$$

with $x = D_{\rm stiff}Q^2/k_{\rm B}T$. In the presence of energy gap Δ in the magnon spectra, the variable x changes to $x = (\Delta + D_{\rm stiff}Q^2)/k_{\rm B}T$ and the formula for internal energy is changed to

$$U_{\rm mag} = \frac{1}{4\pi^2 D^{3/2}_{\rm stiff}}\int\frac{E(E-\Delta)^{1/2}}{e^x - 1}dE. \tag{4}$$

The specific heat for a magnon is the temperature derivative of the energy, as

$$C_{\rm mag} = \frac{\partial U_{\rm mag}}{\partial T}. \tag{5}$$

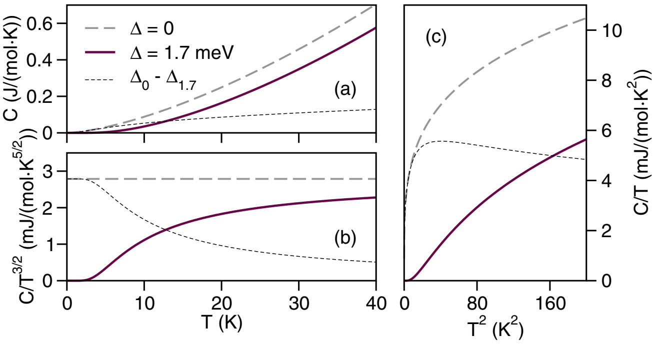

FIG. 8. Magnon specific heat of the NCL*a* phase with $U = 1$ eV and $\eta = 2.3$. The plots of (a) C vs T, (b) $C/T^{3/2}$ vs T, and (c) C/T vs T^2 are obtained with $D_{\rm stiff} = 64.34$ meVÅ^2 using Eq. (5).

The total contribution to the specific heat is

$$C_{\rm tot} = C_{\rm el} + C_{\rm ph} + C_{\rm mag}, \tag{6}$$

where $C_{\rm el}$, $C_{\rm ph}$, and $C_{\rm mag}$ are contributions from the electrons, phonons, and magnons, being distinguished by their low-temperature terms of γT, βT^3, and $\delta T^{3/2}$, respectively.

Figure 8 shows the plots of calculated magnon specific heat for $\Delta = 0$ and 1.7 meV using Eq. (5). In the C versus T plot [Fig. 8(a)], the difference between the two cases is not easily resolved. However, the $C/T^{3/2}$ versus T plot [Fig. 8(b)] shows the main difference of the two cases, namely that the integral in Eq. (5) is independent of temperature for $\Delta = 0$, while it is increasing for $\Delta > 0$. Figure 8(c) shows the $C/T = \gamma + \beta T^2 + \delta T^{1/2}$ versus T^2 dependence, which is usually employed in the analysis of the experimental data in order to get the linear contributions of γ and β and distinguish the magnon contribution as a deviation from the linearity. In the case of metallic ferromagnet SrRuO$_3$, the low-temperature specific heat is dominated by an electronic contribution characterized by the an experimentally determined coefficient $\gamma \sim 30$–36 mJ mol^{-1} K^{-2} [43,44,51,52], whereas with increasing temperature the lattice contribution βT^3 becomes prevailing. Nevertheless, the calculated magnon contribution at, e.g., 10 K would make about 20% for $\Delta = 0$ and 13% for $\Delta = 1.7$ meV compared to the sum of electron and phonon contributions to the specific heat. This means that the cases for $\Delta = 0$ and $\Delta > 0$ could be resolved and the gap in the magnon spectra could be experimentally determined. Let us note that for insulating ferromagnets with $\gamma = 0$, the magnon contribution would be dominant at low temperature, and the determination of a possible magnon gap could be more accurate.

IV. CONCLUSIONS

In the present work, we have analyzed SOC effects on canting of the ferromagnetic configuration of SrRuO$_3$ in dependence on the RuO$_6$ octahedral tilting, and we investigated the influence of this canting on the electronic structure and magnon spectra. The results of LDA+U calculations with $U = 1$ eV show a good agreement with the experimental data on the magnetic moment, the absence of a gap in the spin-up channel, and the correct easy-axis along the *a*-axis of the *Pbnm* perovskite structure. The canted spin moments at Ru^{4+} sites, obtained upon the SOC inclusion, create certain long-range order that can be described as a superposition of the *C*-type AFM component along the *b*- and *G*-type AFM components along *c*. Together with the main FM component along *a*, this gives a noncollinear configuration of the magnetic group symmetry $Pbm'n'$. The total magnetic moment of $\mathrm{SrRuO_3}$ has been calculated to $1.75\mu_\mathrm{B}$ per f.u., and the local spin and orbital moments for the Ru(1) site at crystallographic position [1/2, 0, 0] are quantified by vectors $g_S\mathbf{S} = [1.285, -0.063, -0.073]\mu_\mathrm{B}$ and $g_L\tilde{\mathbf{L}} = [0.023, 0.001, 0.008]\mu_\mathrm{B}$. Spin-orbit coupling has only a marginal effect with regard to the metallic character of the compound and the energy-dependent densities of states.

To illustrate the character of Ru^{4+} local electronic states and the nature of the nonzero orbital moment, we note that diagonalization of the density matrix, calculated for the collinear FM model of $\mathrm{SrRuO_3}$ by LDA+U in the absence SOC, defines ten real-valued eigenvectors of 4*d* electrons in the full local basis d_{xy}, d_{yz}, d_{xz}, $d_{x^2-y^2}$, and $d_{3z^2-r^2}$. They form altogether a nearly fully occupied $t_{2g}(\uparrow)$ triplet, a partially occupied $t_{2g}(\downarrow)$ triplet, and a small number of $e_g(\uparrow)$ and $e_g(\downarrow)$ doublets. The charge density distribution of 4*d* electrons is cubic symmetrical. In the present case of noncollinear LDA+U calculations with SOC, the eigenvectors are complex-valued with some spin-up/-down mixing, but analogous triplets and doublets can still be identified. The most important effect of SOC is detected for three eigenstates that form the triplet of essentially $t_{2g}(\downarrow)$ character and unquenched orbital momentum. The occupation numbers are now differentiated, making 0.634:0.602:0.581 in contrast to nearly identical numbers 0.605:0.604:0.600 for the triplet calculated without SOC. We thus conclude that the above-mentioned nonzero orbital momentum of Ru^{4+} arises as a consequence of such an unlikely occupation of $t_{2g}(\downarrow)$ eigenvectors of fictitious momentum $\tilde{L}_z = \pm 1, 0$, whereas the calculated charge density distribution remains cubic symmetrical or very close to this.

The other part of the present work has been devoted to the determination of magnetic exchange interactions between the nearest and next-nearest Ru^{4+} neighbors, based on LDA+U+SOC calculation. The results point to a significant contribution of the anisotropic and Dzyaloshinskii-Moriya interactions in addition to the isotropic Heisenberg term. The calculated exchange parameters have allowed us to determine and interpret the magnon spectra in $\mathrm{SrRuO_3}$. It appears that the experimental data on the magnon gap are well reproduced, and the stiffness constant and Curie temperature 165 K can be fitted by means of the scale factor $\eta = 2.3$ that also matches the renormalization of the calculated electronic bandwidth. Finally, the effect of a magnon gap has been analyzed with respect to its possible manifestation in the low-temperature specific heat measurements of ferromagnets.

ACKNOWLEDGMENTS

The financial support from the Czech Science Foundation Project No. 19-06433S and the National Research Foundation of Korea No. NRF2019R1A2C1009588 are acknowledged. Computational resources were supplied by the project e-Infrastruktura CZ (e-INFRA CZ LM2018140) supported by the Ministry of Education, Youth and Sports of the Czech Republic.

---

[1] B. J. Kim, H. Ohsumi, T. Komesu, S. Sakai, T. Morita, H. Takagi, and T. Arima, Phase-sensitive observation of a spin-orbital Mott state in $\mathrm{Sr_2\,IrO_4}$, Science **323**, 1329 (2009).

[2] G. Jackeli and G. Khaliullin, Mott Insulators in the Strong Spin-Orbit Coupling Limit: From Heisenberg to a Quantum Compass and Kitaev Models, Phys. Rev. Lett. **102**, 017205 (2009).

[3] I. V. Solovyev, N. Hamada, and K. Terakura, Non-collinear magnetism in distorted perovskite compounds, Phys. B **237-238**, 44 (1997).

[4] I. V. Solovyev, Effect of the orthorhombic distortion on the magneto-optical properties of $\mathrm{SrRuO_3}$, J. Magn. Magn. Mater. **177-181**, 811 (1998).

[5] F. R. Lux, F. Freimuth, S. Blügel, and Y. Mokrousov, Chiral Hall Effect in Noncollinear Magnets from a Cyclic Cohomology Approach, Phys. Rev. Lett. **124**, 096602 (2020).

[6] J. Kipp, K. Samanta, F. R. Lux, M. Merte, D. Go, J.-P. Hanke, M. Redies, F. Freimuth, S. Blügel, M. Ležaić, and Y. Mokrousov, The chiral Hall effect in canted ferromagnets and antiferromagnets, Commun. Phys. **4**, 99 (2021).

[7] S. Kunkemöller, D. Brüning, A. Stunault, A. A. Nugroho, T. Lorenz, and M. Braden, Magnetic shape-memory effect in $\mathrm{SrRuO_3}$, Phys. Rev. B **96**, 220406 (2017).

[8] K. Jenni, S. Kunkemöller, D. Brüning, T. Lorenz, Y. Sidis, A. Schneidewind, A. A. Nugroho, A. Rosch, D. I. Khomskii, and M. Braden, Interplay of Electronic and Spin Degrees in Ferromagnetic $\mathrm{SrRuO_3}$: Anomalous Softening of the Magnon Gap and Stiffness, Phys. Rev. Lett. **123**, 017202 (2019).

[9] C. W. Jones, P. D. Battle, P. Lightfoot, and W. T. A. Harrison, The structure of $\mathrm{SrRuO_3}$ by time-of-flight neutron powder diffraction, Acta Cryst. C **45**, 365 (1989).

[10] B. C. Chakoumakos, S. E. Nagler, S. T. Misture, and H. M. Christen, High-temperature structural behavior of $\mathrm{SrRuO_3}$, Phys. B **241-243**, 358 (1997).

[11] B. J. Kennedy and B. A. Hunter, High-temperature phases of $\mathrm{SrRuO_3}$, Phys. Rev. B **58**, 653 (1998).

[12] J. S. Gardner, G. Balakrishnan, and D. McK. Paul, Neutron powder diffraction studies of $\mathrm{Sr_2\,RuO_4}$ and $\mathrm{SrRuO_3}$, Physica C **252**, 303 (1995).

[13] S. N. Bushmeleva, V. Y. Pomjakushin, E. V. Pomjakushina, D. V. Sheptyakov, and A. M. Balagurov, Evidence for the band ferromagnetism in $\mathrm{SrRuO_3}$ from neutron diffraction, J. Magn. Magn. Mater. **305**, 491 (2006).

[14] S. Lee, J. R. Zhang, S. Torii, S. Choi, D.-Y. Cho, T. Kamiyama, J. Yu, K. A. McEwen, and J.-G. Park, Large in-plane deformation of $\mathrm{RuO_6}$ octahedron and ferromagnetism of bulk $\mathrm{SrRuO_3}$, J. Phys.: Condens. Matter **25**, 465601 (2013).

[15] A. M. Glazer, The classification of tilted octahedra in perovskites, Acta Cryst. B **28**, 3384 (1972).

[16] Y. Nakamura, The invar problem, IEEE Trans. Magn. **12**, 278 (1976).

[17] T. Kiyama, K. Yoshimura, K. Kosuge, Y. Ikeda, and Y. Bando, Invar effect of $SrRuO_3$: Itinerant electron magnetism of Ru 4*d* electrons, Phys. Rev. B **54**, R756(R) (1996).

[18] S. Itoh, Y. Endoh, T. Yokoo, D. Kawana, Y. Kaneko, Y. Tokura, and M. Fujita, Neutron Brillouin scattering with pulsed spallation neutron source—Spin-wave excitations from ferromagnetic powder samples, J. Phys. Soc. Jpn. **82**, 043001 (2013).

[19] S. Itoh, Y. Endoh, T. Yokoo, S. Ibuka, J.-G. Park, Y. Kaneko, K. S. Takahashi, Y. Tokura, and N. Nagaosa, Weyl fermions and spin dynamics of metallic ferromagnet $SrRuO_3$, Nat. Commun. **7**, 11788 (2016).

[20] Z. Fang, N. Nagaosa, K. S. Takahashi, A. Asamitsu, R. Mathieu, T. Ogasawara, H. Yamada, M. Kawasaki, Y. Tokura, and K. Terakura, The anomalous Hall effect and magnetic monopoles in momentum space, Science **302**, 92 (2003).

[21] G. D. Dwivedi, C.-M. Wu, B.-Y. Chen, S. T. Lin, W.-Z. Qiu, S. J. Sun, G. Xu, J. W. Lynn, J. W. Chiou, C.-H. Lee *et al.*, Magnon profile on $SrRuO_3$ films studied by inelastic neutron scattering, Phys. Rev. B **101**, 054403 (2020).

[22] A. Abragam and B. Bleaney, *Electron Paramagnetic Resonance of Transition Ions* (Clarendon Press, Oxford, 1970).

[23] Z. Jirák, Group-theoretical approach to orbital ordering in crystals with E_g and T_{2g} ions, Phys. Rev. B **46**, 8725 (1992).

[24] M. S. Sturge, The Jahn-Teller effect in solids, in *Solid State Physics, Advances in Research and Applications* (Academic Press, New York, 1967).

[25] D. I. Khomskii and S. V. Streltsov, Orbital effects in solids: Basics, recent progress, and opportunities, Chem. Rev. **121**, 2992 (2021).

[26] G. Kresse and J. Furthmüller, Efficiency of ab-initio total energy calculations for metals and semiconductors using a plane-wave basis set, Comput. Mater. Sci. **6**, 15 (1996).

[27] G. Kresse and J. Furthmüller, Efficient iterative schemes for ab initio total-energy calculations using a plane-wave basis set, Phys. Rev. B **54**, 11169 (1996).

[28] G. Kresse and J. Joubert, From ultrasoft pseudopotentials to the projector augmented wave method, Phys. Rev. B **59**, 1758 (1999).

[29] D. M. Ceperley and B. J. Alder, Ground State of the Electron Gas by a Stochastic Method, Phys. Rev. Lett. **45**, 566 (1980).

[30] V. I. Anisimov, I. V. Solovyev, M. A. Korotin, M. T. Czyżyk, and G. A. Sawatzky, Density-functional theory and NiO photoemission spectra, Phys. Rev. B **48**, 16929 (1993).

[31] D. Hobbs, G. Kresse, and J. Hafner, Fully unconstrained noncollinear magnetism within the projector augmented-wave method, Phys. Rev. B **62**, 11556 (2000).

[32] A. A. Mostofi, J. R. Yates, G. Pizzi, Y.-S. Lee, I. Souza, D. Vanderbilt, and N. Marzari, An updated version of wannier90: A tool for obtaining maximally-localised Wannier functions, Comput. Phys. Commun. **185**, 2309 (2014).

[33] X. He, N. Helbig, M. J. Verstraete, and E. Bousquet, TB2J: A python package for computing magnetic interaction parameters, Comput. Phys. Commun. **264**, 107938 (2021).

[34] P. Depondt and F. G. Mertens, Spin dynamics simulations of two-dimensional clusters with Heisenberg and dipole-dipole interactions, J. Phys.: Condens. Matter **21**, 336005 (2009).

[35] X. Gonze, B. Amadon, G. Antonius, F. Arnardi, L. Baguet, J.-M. Beuken, J. Bieder, F. Bottin, J. Bouchet, E. Bousquet *et al.*, The ABINIT project: Impact, environment and recent developments, Comput. Phys. Commun. **248**, 107042 (2020).

[36] A. H. Romero, D. C. Allan, B. Amadon, G. Antonius, T. Applencourt, L. Baguet, J. Bieder, F. Bottin, J. Bouchet, E. Bousquet *et al.*, ABINIT: Overview, and focus on selected capabilities, J. Chem. Phys. **152**, 124102 (2020).

[37] S. Toth and B. Lake, Linear spin wave theory for single-Q incommensurate magnetic structures, J. Phys.: Condens. Matter **27**, 166002 (2015).

[38] S. Petit, Numerical simulations and magnetism, Collection SFN **12**, 105 (2011).

[39] See Supplemental Material at http://link.aps.org/supplemental/10.1103/PhysRevB.105.245107 for the density matrix, the charge density plot, the electronic structure, the magnetic coupling constants with respect to the distance, and the effects of η, J^{iso}, $\mathbf{J}^{\mathrm{ani}}$, and $\vec{D}$ on the magnon dispersion.

[40] E. O. Wollan and W. C. Koehler, Neutron diffraction study of the magnetic properties of the series of perovskite-type compounds $[(1-{-x})\mathrm{La}, x\mathrm{Ca}]\mathrm{MnO}_3$, Phys. Rev. **100**, 545 (1955).

[41] S. Kunkemöller, K. Jenni, D. Gorkov, A. Stunault, S. Streltsov, and M. Braden, Magnetization density distribution in the metallic ferromagnet $SrRuO_3$ determined by polarized neutron diffraction, Phys. Rev. B **100**, 054413 (2019).

[42] T. Moriya, *Spin Fluctuations in Itinerant Electron Magnetism* (Springer-Verlag, Berlin, Heidelberg, 1985).

[43] P. Tomeš, K. Knížek, A. Weidenkaff, and J. Hejtmánek, On the physical properties of $Sr_{1-x}Na_xRuO_3$ ($x = 0 - 0.19$), Solid State Sci. **12**, 1112 (2010).

[44] N. Kikugawa, R. Baumbach, J. S. Brooks, T. Terashima, S. Uji, and Y. Maeno, Single-crystal growth of a perovskite ruthenate $SrRuO_3$ by the floating-zone method, Cryst. Growth Des. **15**, 5573 (2015).

[45] I. Souza, N. Marzari, and D. Vanderbilt, Maximally localized Wannier functions for entangled energy bands, Phys. Rev. B **65**, 035109 (2001).

[46] O. Grånäs, I. Di Marco, O. Eriksson, L. Nordström, and C. Etz, Electronic structure, cohesive properties, and magnetism of $SrRuO_3$, Phys. Rev. B **90**, 165130 (2014).

[47] M. Kim and B. I. Min, Nature of itinerant ferromagnetism of $SrRuO_3$: A DFT+DMFT study, Phys. Rev. B **91**, 205116 (2015).

[48] S. Hahn, B. Sohn, M. Kim, J. R. Kim, S. Huh, Y. Kim, W. Kyung, M. Kim, D. Kim, Y. Kim *et al.*, Observation of Spin-Dependent Dual Ferromagnetism in Perovskite Ruthenates, Phys. Rev. Lett. **127**, 256401 (2021).

[49] X. Zhu, A. Edström, and C. Ederer, Magnetic exchange interactions in $SrMnO_3$, Phys. Rev. B **101**, 064401 (2020).

[50] C. Kittel, *Quantum Theory of Solids* (Wiley, New York, 1987).

[51] T. Kiyama, K. Yoshimura, K. Kosuge, H. Michor, and G. Hilscher, Specific heat of $(\mathrm{Sr}-\mathrm{Ca})\mathrm{RuO}_3$, J. Phys. Soc. Jpn. **67**, 307 (1998).

[52] J. Okamoto, T. Mizokawa, A. Fujimori, I. Hase, M. Nohara, H. Takagi, Y. Takeda, and M. Takano, Correlation effects in the electronic structure of $SrRuO_3$, Phys. Rev. B **60**, 2281 (1999).